Research Article | Vol. 26, No. 7 | 2 Apr 2018 | OPTICS EXPRESS 8968
Optics EXPRESS

Retrieval of aerosol properties and water-leaving reflectance from multi-angular polarimetric measurements over coastal waters

MENG GAO,[1,*] PENG-WANG ZHAI,[1] BRYAN FRANZ,[2] YONGXIANG HU,[3] KIRK KNOBELSPIESSE,[2] P. JEREMY WERDELL,[2] AMIR IBRAHIM,[2] FENG XU,[4] AND BRIAN CAIRNS[5]

[1]*JCET, Physics Department, University of Maryland, Baltimore County, Baltimore, MD 21250, USA*
[2]*NASA Goddard Space Flight Center, Code 616, Greenbelt, Maryland 20771, USA*
[3]*MS 475 NASA Langley Research Center, Hampton, VA 23681-2199, USA*
[4]*Jet Propulsion Laboratory, California Institute of Technology, Pasadena, CA 91109, USA*
[5]*NASA Goddard Institute for Space Studies, New York, NY 10025, USA*
[*]*mgao@umbc.edu*

Abstract: Ocean color remote sensing is an important tool to monitor water quality and biogeochemical conditions of ocean. Atmospheric correction, which obtains water-leaving radiance from the total radiance measured by satellite-borne or airborne sensors, remains a challenging task for coastal waters due to the complex optical properties of aerosols and ocean waters. In this paper, we report a research algorithm on aerosol and ocean color retrieval with emphasis on coastal waters, which uses coupled atmosphere and ocean radiative transfer model to fit polarized radiance measurements at multiple viewing angles and multiple wavelengths. Ocean optical properties are characterized by a generalized bio-optical model with direct accounting for the absorption and scattering of phytoplankton, colored dissolved organic matter (CDOM) and non-algal particles (NAP). Our retrieval algorithm can accurately determine the water-leaving radiance and aerosol properties for coastal waters, and may be used to improve the atmospheric correction when apply to a hyperspectral ocean color instrument.

OCIS codes: (010.4450) Oceanic optics; (010.0280) Remote sensing and sensors; (010.1285) Atmospheric correction.

References and links

1. D. V. Chapman, *Water quality assessments: a guide to the use of biota, sediments and water in environmental monitoring* (World Health Organization, 1996).
2. J. E. Bauer, W.-J. Cai, P. A. Raymond, T. S. Bianchi, C. S. Hopkinson, and P. A. G. Regnier, "The changing carbon cycle of the coastal ocean," Nature **504**(7478), 61–70 (2013).
3. C. D. G. Harley, A. Randall Hughes, K. M. Hultgren, B. G. Miner, C. J. B. Sorte, C. S. Thornber, L. F. Rodriguez, L. Tomanek, and S. L. Williams, "The impacts of climate change in coastal marine systems," Ecol. Lett. **9**(2), 228–241 (2006).
4. IOCCG, "Missions & Instruments," http://ioccg.org/resources/missions-instruments/ (2017).
5. S. Sathyendranath, "Remote sensing of ocean colour in coastal, and other optically-complex, waters," IOCCG Report Number3, 1–145 (2000).
6. M. Wang, "Atmospheric correction for remotely-sensed ocean-colour products," Reports of International Ocean-Color Coordinating Group No. 10, IOCCG pp. 1–83 (2009).
7. H. R. Gordon, T. Du, and T. Zhang, "Remote sensing of ocean color and aerosol properties: resolving the issue of aerosol absorption," Appl. Opt. **36**(33), 8670–8684 (1997).
8. F. Zhao and T. Nakajima, "Simultaneous determination of water-leaving reflectance and aerosol optical thickness from Coastal Zone Color Scanner measurements," Appl. Opt. **36**(27), 6949–6956 (1997).
9. R. M. Chomko and H. R. Gordon, "Atmospheric correction of ocean color imagery: use of the junge power-law aerosol size distribution with variable refractive index to handle aerosol absorption," Appl. Opt. **37**(24), 5560–5572 (1998).
10. R. M. Chomko and H. R. Gordon, "Atmospheric correction of ocean color imagery: test of the spectral optimization algorithm with the Sea-viewing Wide Field-of-View Sensor," Appl. Opt. **40**(18), 2973–2984 (2001).
11. K. Stamnes, W. Li, B. Yan, H. Eide, A. Barnard, W. S. Pegau, and J. J. Stamnes, "Accurate and self-consistent ocean color algorithm: simultaneous retrieval of aerosol optical properties and chlorophyll concentrations," Appl. Opt.

#319056 https://doi.org/10.1364/OE.26.008968
Journal © 2018 Received 8 Jan 2018; revised 20 Mar 2018; accepted 21 Mar 2018; published 28 Mar 2018

Optics EXPRESS

42(6), 939–951 (2003).
12. M. Wang and W. Shi, "The NIR-SWIR combined atmospheric correction approach for MODIS ocean color data processing," Opt. Express **15**(24), 15722–15733 (2007).
13. P. J. Werdell, B. A. Franz, and S. W. Bailey, "Evaluation of shortwave infrared atmospheric correction for ocean color remote sensing of Chesapeake Bay," Remote Sens. Environ. **114**(10), 2238–2247 (2010).
14. S. W. Bailey, B. A. Franz, and P. J. Werdell, "Estimation of near-infrared water-leaving reflectance for satellite ocean color data processing," Opt. Express **18**(7), 7521–7527 (2010).
15. X. He, Y. Bai, D. Pan, J. Tang, and D. Wang, "Atmospheric correction of satellite ocean color imagery using the ultraviolet wavelength for highly turbid waters," Opt. Express **20**(18), 20754–20770 (2012).
16. Y. Fan, W. Li, C. K. Gatebe, C. Jamet, G. Zibordi, T. Schroeder, and K. Stamnes, "Atmospheric correction over coastal waters using multilayer neural networks," Remote Sens. Environ. **199**, 218–240 (2017).
17. R. Doerffer and J. Fischer, "Concentrations of chlorophyll, suspended matter, and gelbstoff in case II waters derived from satellite coastal zone color scanner data with inverse modeling methods," J. Geophys. Res.: Atmos. **99**(C4), 7457–7466 (1994).
18. C. P. Kuchinke, H. R. Gordon, and B. A. Franz, "Spectral optimization for constituent retrieval in Case 2 waters I: Implementation and performance," Remote Sens. Environ. **113**(3), 571–587 (2009).
19. C. P. Kuchinke, H. R. Gordon, L. W. Harding, Jr, and K. J. Voss, "Spectral optimization for constituent retrieval in Case 2 waters II: Validation study in the Chesapeake Bay," Remote Sens. Environ. **113**(3), 610–621 (2009).
20. C. Shi, T. Nakajima, and M. Hashimoto, "Simultaneous retrieval of aerosol optical thickness and chlorophyll concentration from multiwavelength measurement over East China Sea," J. Geophys. Res.: Atmos. **121**(23), 14,084–14,101 (2016).
21. P. Y. Deschamps, F. M. Breon, M. Leroy, A. Podaire, A. Bricaud, J. C. Buriez, and G. Seze, "The POLDER mission: instrument characteristics and scientific objectives," IEEE Trans. Geosci. Remote Sens. **32**(3), 598–615 (1994).
22. B. Cairns, E. E. Russell, and L. D. Travis, "Research scanning polarimeter: calibration and ground-based measurements," Proc. SPIE **3754**, 1–11 (1999).
23. D. J. Diner, F. Xu, M. J. Garay, J. V. Martonchik, B. E. Rheingans, S. Geier, A. Davis, B. R. Hancock, V. M. Jovanovic, M. A. Bull, K. Capraro, R. A. Chipman, and S. C. McClain, " The Airborne Multiangle SpectroPolarimetric Imager (AirMSPI): a new tool for aerosol and cloud remote sensing," Atmos. Meas. Tech. **6**(8), 2007–2025 (2013).
24. F. Snik, J. H. H. Rietjens, G. van Harten, D. M. Stam, C. U. Keller, J. M. Smit, E. C. Laan, A. L. Verlaan, R. ter Horst, R. Navarro, K. Wielinga, S. G. Moon, and R. Voors, "SPEX: the spectropolarimeter for planetary exploration," in SPIE Astronomical Telescopes + Instrumentation, J. M. Oschmann, Jr, M. C. Clampin, and H. A. MacEwen, eds. (SPIE, 2010), p. 77311B.
25. J. V. Martins, T. Nielsen, C. Fish, L. Sparr, R. Fernandez-Borda, M. Schoeberl, and L. Remer, "HARP CubeSat–An innovative hyperangular imaging polarimeter for earth science applications," Small Sat Pre-Conference Workshop, Logan Utah (2014).
26. J. Chowdhary, B. Cairns, M. I. Mishchenko, P. V. Hobbs, G. F. Cota, J. Redemann, K. Rutledge, B. N. Holben, and E. Russell, "Retrieval of aerosol scattering and absorption properties from photopolarimetric observations over the ocean during the CLAMS experiment," J. Atmos. Sci. **62**(4), 1093–1117 (2005).
27. O. P. Hasekamp, P. Litvinov, and A. Butz, "Aerosol properties over the ocean from PARASOL multiangle photopolarimetric measurements," J. Geophys. Res.: Oceans **116**(D14), D14204 (2011).
28. F. Xu, O. Dubovik, P. W. Zhai, D. J. Diner, O. V. Kalashnikova, F. C. Seidel, P. Litvinov, A. Bovchaliuk, M. J. Garay, G. van Harten, and A. B. Davis, "Joint retrieval of aerosol and water-leaving radiance from multispectral, multiangular and polarimetric measurements over ocean," Atmos. Meas. Tech. **9**(7), 2877–2907 (2016).
29. K. Knobelspiesse, B. Cairns, M. Mishchenko, J. Chowdhary, K. Tsigaridis, B. van Diedenhoven, W. Martin, M. Ottaviani, and M. Alexandrov, "Analysis of fine-mode aerosol retrieval capabilities by different passive remote sensing instrument designs," Opt. Express **20**(19), 21457–21484 (2012).
30. PACE, *Pre-Aerosol,Clouds, and ocean Ecosystem (PACE) Mission Science Definition Team Report* (NASA, 2012).
31. J. J. Moré, "The Levenberg–Marquardt algorithm: implementation and theory," in Lecture Notes in Mathematics: Numerical Analysis,Proceedings of the Biennial Conference Held at Dundee, G. A. Watson, ed. (Berlin: Springer-Verlag, 1977), pp. 105–116.
32. J. J. Moré, B. S. Garbow, and K. E. Hillstrom, *User Guide for MINPACK-1* (Argonne National Laboratory Report ANL-80-74, Argonne, Ill, 1980).
33. C. D. Mobley, J. Werdell, B. Franz, Z. Ahmad, and S. Bailey, *Atmospheric Correction for Satellite Ocean Color Radiometry* (National Aeronautics and Space Administration, 2016).
34. C. D. Rodgers, *Inverse Methods for Atmospheric Sounding:Theory and Practice* (World Scientific Publishing, 2000).
35. P.-W. Zhai, Y. Hu, C. A. Hostetler, B. Cairns, R. A. Ferrare, K. D. Knobelspiesse, D. B. Josset, C. R. Trepte, P. L. Lucker, and J. Chowdhary, "Uncertainty and interpretation of aerosol remote sensing due to vertical inhomogeneity," J. Quant. Spectrosc. Radiat. Transfer **114**, 91–100 (2013).
36. F. Waquet, J. Riedi, L. C. Labonnote, P. Goloub, B. Cairns, J. L. Deuzé, and D. Tanré, "Aerosol remote sensing over clouds using A-Train observations," J. Atmos. Sci. **66**(8), 2468–2480 (2009).
37. P.-W. Zhai, Y. Hu, C. R. Trepte, and P. L. Lucker, "A vector radiative transfer model for coupled atmosphere and ocean systems based on successive order of scattering method," Opt. Express **17**(4), 2057–2079 (2009).
38. P.-W. Zhai, Y. Hu, J. Chowdhary, C. R. Trepte, P. L. Lucker, and D. B. Josset, "A vector radiative transfer model for

Optics EXPRESS

coupled atmosphere and ocean systems with a rough interface," J. Quant. Spectrosc. Radiat. Transfer **111**, 1025–1040 (2010).
39. P.-W. Zhai, Y. Hu, D. M. Winker, B. A. Franz, J. Werdell, and E. Boss, "Vector radiative transfer model for coupled atmosphere and ocean systems including inelastic sources in ocean waters," Opt. Express **25**(8), A223–A239 (2017).
40. Committee on Extension to the Standard Atmosphere, *U. S. standard atmosphere* (U.S. Government Printing Office,Washington D.C., 1976).
41. J. E. Hansen and L. D. Travis, "Light scattering in planetary atmospheres," Space Sci. Rev. **16**(4), 527–610 (1974).
42. M. I. Mishchenko, L. D. Travis, and A. A. Lacis, *Scattering, Absorption, and Emission of Light by Small Particles* (Cambridge University Press, 2002).
43. A. Hyvärinen, J. Karhunen, and E. Oja, *Independent Component Analysis* (Wiley, 2001).
44. E. P. Shettle and R. W. Fenn, "Models for the aerosols of the lower atmosphere and the effects of humidity variations on their optical properties," Environmental Research Papers, Air Force Geophysics Lab., Hanscom AFB, MA. Optical Physics Div. (1979).
45. G. A. D'Almeida, P. Koepke, and E. P. Shettle, Atmospheric aerosols: Global climatology and radiative characteristics (A. Deepak Pub., Hampton, Va., USA, 1991).
46. L. Wu, O. Hasekamp, B. van Diedenhoven, and B. Cairns, "Aerosol retrieval from multiangle, multispectral photopolarimetric measurements: importance of spectral range and angular resolution," Atmos. Meas. Tech. **8**(6), 2625–2638 (2015).
47. Z. Ahmad, B. A. Franz, C. R. McClain, E. J. Kwiatkowska, J. Werdell, E. P. Shettle, and B. N. Holben, "New aerosol models for the retrieval of aerosol optical thickness and normalized water-leaving radiances from the SeaWiFS and MODIS sensors over coastal regions and open oceans," Appl. Opt. **49**(29), 5545–5560 (2010).
48. M. Gao, Y. You, P. Yang, and G. W. Kattawar, "Backscattering properties of small layered plates: a model for iridosomes," Opt. Express **20**(22), 25111–25120 (2012).
49. G. W. Kattawar and G. N. Plass, "Interior radiances in optically deep absorbing media—I Exact solutions for one-dimensional model," J. Quant. Spectrosc. Radiat. Transfer **13**(11), 1065–1080 (1973).
50. M. Gao, X. Huang, P. Yang, and G. W. Kattawar, "Angular distribution of diffuse reflectance from incoherent multiple scattering in turbid media," Appl. Opt. **52**(24), 5869–5879 (2013).
51. C. Cox and W. Munk, "Measurement of the roughness of the sea surface from photographs of the sun's glitter," J. Opt. Soc. Am. **44**(11), 838–850 (1954).
52. L. Kou, D. Labrie, and P. Chylek, "Refractive indices of water and ice in the 0.65- to 2.5-μm spectral range," Appl. Opt. **32**(19), 3531–3540 (1993).
53. R. M. Pope and E. S. Fry, "Absorption spectrum (380–700 nm) of pure water. II. Integrating cavity measurements," Appl. Opt. **36**(33), 8710–8723 (1997).
54. X. Zhang and L. Hu, "Scattering by pure seawater at high salinity," Opt. Express **17**(15), 12685–12691 (2009).
55. A. Morel, "Optical properties of pure water and pure sea water," in Optical Aspects of Oceanography, N. G. Jerlov and E. Steemann Nielson, eds. (Academic Press, New York, 1974), pp. 1–24.
56. A. Bricaud, A. Morel, M. Babin, K. Allali, and H. Claustre, "Variations of light absorption by suspended particles with chlorophyll a concentration in oceanic (case 1) waters: Analysis and implications for bio-optical models," J. Geophys. Res.: Oceans **103**(C13), 31033–31044 (1998).
57. D. Stramski, E. Boss, D. Bogucki, and K. J. Voss, "The role of seawater constituents in light backscattering in the ocean," Prog. Oceanogr. **61**(1), 27–56 (2004).
58. Y. Huot, A. Morel, M. S. Twardowski, D. Stramski, and R. A. Reynolds, "Particle optical backscattering along a chlorophyll gradient in the upper layer of the eastern South Pacific Ocean," Biogeosciences **5**(2), 495–507 (2008).
59. Z. Lee, *Remote Sensing of Inherent Optical Properties: Fundamentals, Tests of Algorithms, and Applications*, IOCCG Report Number 5 (2006).
60. P. J. Werdell, B. A. Franz, S. W. Bailey, G. C. Feldman, E. Boss, V. E. Brando, M. Dowell, T. Hirata, S. J. Lavender, Z. Lee, H. Loisel, S. E. P. Maritorena, F. E. d' Melin, T. S. Moore, T. J. Smyth, D. Antoine, E. Devred, O. H. F. d'Andon, and A. Mangin, "Generalized ocean color inversion model for retrieving marine inherent optical properties," Appl. Opt. **52**(10), 2019–2037 (2013).
61. P. J. Werdell, L. I. W. McKinna, E. Boss, S. G. Ackleson, S. E. Craig, W. W. Gregg, Z. Lee, S. Maritorena, C. S. Roesler, C. S. Rousseaux, D. Stramski, J. M. Sullivan, M. S. Twardowski, M. Tzortziou, and X. Zhang, "An overview of approaches and challenges for retrieving marine inherent optical properties from ocean color remote sensing," Prog. Oceanogr. **160**, 186–212 (2018).
62. G. R. Fournier and J. L. Forand, "Analytic phase function for ocean water," Proc. SPIE **2258**, 194–201 (1994).
63. J. M. Sullivan and M. S. Twardowski, "Angular shape of the oceanic particulate volume scattering function in the backward direction," Appl. Opt. **48**(35), 6811–6819 (2009).
64. C. D. Mobley, L. K. Sundman, and E. Boss, "Phase function effects on oceanic light fields," Appl. Opt. **41**(6), 1035–1050 (2002).
65. K. J. Voss and E. S. Fry, "Measurement of the Mueller matrix for ocean water," Appl. Opt. **23**(23), 4427–4439 (1984).
66. A. A. Kokhanovsky, "Parameterization of the Mueller matrix of oceanic waters," J. Geophys. Res.: Oceans **108**(C6), 3175 (2003).
67. F. James, "MINUIT Function Minimization and Error Analysis: Reference Manual Version 94.1," CERN-D-506, CERN-D506 pp. 1–50 (1994).

Optics EXPRESS

68. P.-W. Zhai, K. Knobelspiesse, A. Ibrahim, B. A. Franz, Y. Hu, M. Gao, and R. Frouin, "Water-leaving contribution to polarized radiation field over ocean," Opt. Express **25**(16), A689 (2017).
69. A. Ibrahim, A. Gilerson, J. Chowdhary, and S. Ahmed, "Retrieval of macro- and micro-physical properties of oceanic hydrosols from polarimetric observations," Remote Sens. Environ. **186**, 548–566 (2016).
70. Ocean Color Algorithm Working Group, "Models, parameters, and approaches that used to generate wide range of absorption and backscattering spectra," pp. 1–11 (2003).
71. A. Morel and B. Gentili, "A simple band ratio technique to quantify the colored dissolved and detrital organic material from ocean color remotely sensed data," Remote Sens. Environ. **113**, 998–1011 (2009).
72. M. Babin, D. Stramski, G. M. Ferrari, H. Claustre, A. Bricaud, G. Obolensky, and N. Hoepffner, "Variations in the light absorption coefficients of phytoplankton, nonalgal particles, and dissolved organic matter in coastal waters around Europe," J. Geophys. Res.: Oceans **108**(C7), 3211 (2003).
73. D. Doxaran, K. Ruddick, D. McKee, B. Gentili, D. Tailliez, M. Chami, and M. Babin, "Spectral variations of light scattering by marine particles in coastal waters, from the visible to the near infrared," Limnol. Oceanogr. **54**(4), 1257–1271 (2009).
74. H. R. Gordon, O. B. Brown, R. H. Evans, J. W. Brown, R. C. Smith, K. S. Baker, and D. K. Clark, "A semianalytic radiance model of ocean color," J. Geophys. Res.: Atmos. **93**(D9), 10909–10924 (1988).

1. Introduction

Ocean color remote sensing is critical for monitoring coastal water quality [1] and studying global and regional carbon cycle [2] and coastal marine ecosystem dynamics [3]. In order to achieve global observational capabilities, a series of ocean color missions have been developed and launched by different space agencies [4]. Typical ocean color sensors such as the NASA Moderate Resolution Imaging Spectroradiometer (MODIS) and Visible Infrared Imaging Radiometer Suite (VIIRS), measure the total radiance (L_t; W sr^{-1}m^{-2}nm^{-1}) at the top of the atmosphere (TOA) at multiple wavelengths ranging from deep blue to near infrared or short wave infrared, at a single viewing angle [4].

To obtain water-leaving radiance (L_w; W sr^{-1}m^{-2}nm^{-1}) from the total radiance measurement, algorithms have been developed to remove atmospheric path radiance, a procedure collectively called atmospheric correction. Atmospheric correction has been successful for open oceans, but it remains a challenging task for coastal ocean waters due to the complex optical properties of aerosols and ocean waters in these scenes [5, 6]. Specifically, these include the presence of absorbing aerosols and non-negligible water-leaving radiances in the near infrared (NIR) [6], which challenge our ability to separate the ocean signal from the atmospheric signal. Several atmospheric correction algorithms have been proposed to mitigate these challenging scenarios with mixed success [7–16].

Another approach for atmospheric correction is represented by joint retrieval algorithms, which attempt to determine aerosol and hydrosol properties simultaneously, and have been applied to coastal waters [17–20]. Doerffer et al. [17] applied a two-flow radiative transfer model in an inversion algorithm for the Coastal Zone Color Scanner(CZCS) which retrieved the aerosol path radiance and coastal water constitues: phytoplankton chlorophyll , suspended matter and gelbstoff. Kuchinke et al. [18, 19] extended the spectral optimization algorithm (SOA) to account for both the absorbing aerosols and coastal waters, for applications to SeaWiFS data. Shi et al. [20] proposed a flexible joint inversion algorithm to retrieve aerosol optical thickness (τ_a; unitless) and surface chlorophyll a concentration ($[Chla]$; mg m^{-3}) for both open and coastal waters, which has been applied for the Cloud and Aerosol Imager (CAI) and MODIS images. However, these algorithms have to assume prescribed aerosol models that may not be universally applicable.

Ineffective atmospheric correction over coastal waters is mainly due to insufficient information content in the unpolarized single angle spectral measurements. In the past decade, some multiangle polarimeters have been developed, such as POLDER [21], the Research Scanning Polarimeter(RSP) [22], the Airborne Multiangle SpectroPolarimetric Imager(AirMSPI) [23], the Spectropolarimeter for Planetary EXploration(SPEX) [24] and the HyperAngular Rainbow

Optics EXPRESS

Polarimeter (HARP) [25]. New algorithms have been developed to retrieve aerosol and hydrosol parameters with these multiangle polarimeter datasets [26–28]. These methods generally are joint retrieval algorithms, i.e., the water-leaving signals are simultaneously retrieved with the aerosol properties through an optimization approach.

It has been demonstrated that the multiangle polarimeter observations contain rich information about aerosols and hydrosols and are becoming a powerful new tool for remote sensing of the Earth system [26–29]. Chowdhary et al. [26] have developed a joint retrieval algorithm for the RSP data that retrieves aerosol properties and water optical properties with a bio-optical model parameterized purely by $[Chla]$. Hasekamp et al. [27] have developed a retreival algorithm for PARASOL measurements with a bimodal aerosol model and an ocean model parameterized by $[Chla]$, wind speed and direction, and foam coverage. Xu et al. [28] have included the multi-pixel smoothing constraint in a retrieval algorithm for the AirMSPI dataset, which has greatly improved the robustness of the retrieval algorithm. These algorithms all assume a bio-optical model for open waters whose applicability in coastal waters is limited.

In this paper, we present a joint retrieval algorithm that determines aerosol and hydrosol microphysical properties using multiangle polarimeter data. This algorithm is specifically designed for coastal waters, where traditional $[Chla]$ based bio-optical models break down and aerosol microphysical properties are complicated. The retrieval quantities include the real and imaginary refractive index spectra for both the fine and coarse mode aerosols, the aerosol volume density distribution, wind speed, and ocean optical properties, including the contributions from phytoplankton, colored dissolved organic matter(CDOM) and non-algal particles(NAP). In the retrieval algorithm, a generalized bio-optical model, which synthesize the major optical properties for phytoplankton, CDOM and NAP, has been used to provide an accurate description of coastal water optical properties. The aerosol optical properties, therefore, can be more accurately characterized, and used to improve the atmospheric correction when apply for a hyperspectral ocean color instrument. In this sense, our algorithm may be applied to NASA's PACE (Plankton, Aerosol, Cloud, ocean Ecosystem) mission, which will carry the Ocean Color Instrument (OCI) with continuous wavelength coverage from ultraviolet to near infrared and possibly one or more polarimeters [30].

To evaluate the performance of the approach, synthetic RSP data was generated.The synthetic data is used as input to the retrieval algorithm, and the retrieval parameters are compared to the real parameters that were used to generated the synthetic RSP data. This truth-in and truth-out procedure is used to validate the retrieval algorithm and to understand the retrieval uncertainties associated with each component in the atmosphere and ocean optical model. Both the retrieval and their uncertainties for the aerosol and ocean properties are evaluated. The synthetic RSP data have been generated by our vector radiative transfer model for a coupled atmosphere and ocean system by assuming a bio-optical model for coastal waters which are more accurate but also more complicated than the bio-optical model used in the retrieval algorithm. Though we tested our algorithm using synthetic data with RSP characteristics, it is quite flexible and can be applied to AirMSPI, SPEX, HARP, and other polarimeter data.

The paper is organized in five sections: Section 2 describes the retrieval methodology; Section 3 introduces the synthetic measurement data; Section 4 discusses the retrieval results; and Section 5 summarizes the conclusions. The flow chart for Sections 2-4 is summarized in Fig. 1.

2. Methodology

The retrieval algorithm for the multi-angle polarimeter uses the Levenberg-Marquardt non-linear least square optimization algorithm to minimize a cost function [31, 32]. The cost function for optimization provides a measure of difference between the total and polarized reflectances from the measurement and the forward model. The total reflectance ρ_t and polarized reflectance ρ_Q

Optics EXPRESS

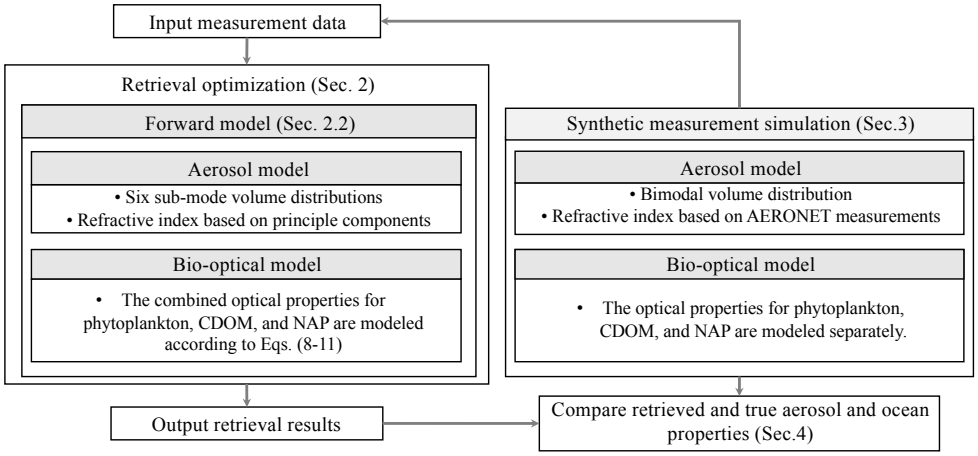

Fig. 1. The flow chart for the retrieval optimization and synthetic measurement simulation. Each model listed in the chart is discussed in details in the corresponding section.

and ρ_U are defined as

$$\rho_t = \pi L_t/[F_0 \cos\theta_0], \quad \rho_Q = \pi Q_t/[F_0 \cos\theta_0], \quad \rho_U = \pi U_t/[F_0 \cos\theta_0], \tag{1}$$

where L_t, Q_t and U_t are the first three Stokes parameters measured at the TOA, which forms the Stokes vector $\mathbf{L}_t = (L_t, Q_t, U_t, V_t)^T$. F_0 is the extraterrestrial solar irradiance, and θ_0 is the solar zenith angle. The total reflectance includes contributions from the Rayleigh(molecular) scattering, aerosol scattering, glint, and whitecaps, as well as the water-leaving contributions [33]. To study the atmospheric correction, the water-leaving reflectance at TOA is defined as $\rho_w^{TOA} = \pi t L_w/[F_0 \cos\theta_0]$, where L_w is the water-leaving radiance just above the ocean surface , and t is the diffuse transmittance from ocean surface to TOA [33]. Therefore, ρ_w^{TOA} is the total reflectance at TOA after removing the contributions from the path radiance of aerosols and molecules, and reflections from glint and whitecaps on the ocean surface.

Both the forward model and the synthetic measurement are designed according to RSP characteristics. The RSP scanning range is within $-60°$ and $60°$ from the nadir with an instantaneous field of view of 14 mrad (0.8°). In our study we chose the viewing zenith angles in the principal plane with the same angular range but a slightly larger resolution of 1°. The negative viewing zenith angles are in the half plane containing the Sun and positive zenith angles are in the half plane containing the glint. If the sun glint measurements is excluded, our tests show that the wind speed retrieval becomes unreliable. The retrieval performance of aerosol properties and water leaving radiance is however not impacted much. Hence the effects of excluding sun glint data are not further discussed in this paper. RSP makes measureaments in 9 bands with 4 visible bands: 410, 470, 550, 670nm, 2 NIR bands: 865 and 960nm, and 3 SWIR bands: 1590, 1880, 2250nm. Currently the two water vapor absorption bands of 960 and 1880nm have been excluded in our study to avoid water vapor uncertainty.

2.1. Cost function

The cost function for the retrieval optimization is defined as the χ^2 function [34, 35]:

$$\chi^2 = \frac{1}{N}\sum_i \left(\frac{[\rho_t(i) - \rho_t^f(\mathbf{x}; i)]^2}{\sigma_t^2(i)} + \frac{[\rho_Q(i) - \rho_Q^f(\mathbf{x}; i)]^2}{\sigma_Q^2(i)} \right) \tag{2}$$

Optics EXPRESS

where i denotes different wavelengths and viewing angles; N is the total number of dimensions with different viewing angles, wavelengths, and polarization states; superscript f indicates the fitted reflectance calculated by the forward model with the state vector $\mathbf{x}$ determined through retrieval. No *a priori* information is involved in the cost function. The measurements are assumed to be in the principal plane in which $\rho_U = 0$ in the cost function. This assumption is, however, can be easily relaxed. The error covariance σ_t and σ_Q in Eq. 2 are defined as

$$\sigma_t^2 = 2\sigma_f^2/\cos^2\theta_0 + \sigma_s\rho_t/\cos\theta_0 + \sigma_c^2\rho_t^2, \tag{3}$$

$$\sigma_Q^2 = 2\sigma_f^2/\cos^2\theta_0 + \sigma_s\rho_t/\cos\theta_0 + \sigma_c^2\rho_Q^2 + \sigma_p^2(\rho_I + |\rho_Q|)^2, \tag{4}$$

where we choose $\sigma_f = 7 \times 10^{-5}$ for the floor noise, $\sigma_s = 7 \times 10^{-8}$ for the shot noise, $\sigma_c = 0.03$ for the calibration uncertainty of radiance and $\sigma_p = 0.002$ for the calibration uncertainty of the degree of polarization [29, 36]. Therefore, the total error for both ρ_t and ρ_Q is dominated by the radiance calibration uncertainty with a value around 3%.

2.2. The forward model for a coupled atmosphere and ocean system

The coupled atmosphere and ocean system is modeled as three uniform layers: 1) a pure molecular (Rayleigh) scattering layer, 2) a Rayleigh-aerosol mixing layer, and 3) an ocean layer. The Stokes vector at TOA is simulated by the Successive Order of Scattering(SOS) radiative transfer code [37–39]. The Rayleigh scattering is modeled through the vertical molecule density profile specified by the 1976 US standard atmosphere [40]. A depolarization of 0.0284 is used to specify the Mueller matrix for molecular scattering [41]. Trace gas absorptions are neglected. Aerosol is approximated as uniformly distributed within 1km from ground. The aerosol phase function and Mueller matrix are calculated from the Mie theory according to the aerosol volume size distribution and refractive index spectrum. The Mie code developed by Mishchenko et al. is used in our retrieval algorithm [42]. The representation of the aerosol refractive index and the volume distribution are discussed below.

Aerosol refractive index usually exhibits spectral dependency. To compute the major spectral variation of the refractive index spectrum, the principal component analysis (PCA) technique [43] is used based on a set of aerosol refractive index spectra from Shettle and Fenn [44, 45]. The refractive index spectra for the fine and coarse mode aerosol can be better represented by separate principal components [46]. The principal components(PCs) for coarse mode are calculated from the refractive index spectra for sea salt, dust and water, while the PCs for the fine mode are calculated from the refractive index spectra for water-soluble, sulfate, mineral, soot and water. The refractive index spectrum is constructed in the form of $m(\lambda) = m_0 + \alpha_1 p_1(\lambda)$, where m_0 is the mean refractive index, $p_1(\lambda)$ is the first order of the principal components, and α_1 is its coefficient. For both real and imaginary parts, two parameters are needed to represent the refractive index spectra, which is equal to four free parameters for each aerosol size mode. A total of eight parameters are therefore required to determine the real and imaginary refractive index spectra for both fine and coarse mode aerosols. After these parameters are determined, the refractive index spectra can be constructed for the seven RSP bands used in this study. For the purpose of atmospheric correction for OCI, the spectra can also be constructed by the same parameters with extended spectral range.

To represent the aerosol volume distribution a combination of six sub-modes each with a log-normal distribution is used:

$$\frac{dv}{d\ln r} = \sum_{i=1}^{6} \frac{V_i}{\sqrt{2\pi}\sigma_i} \exp\left[-\frac{(\ln r - \ln r_i)^2}{2\sigma_i^2}\right] \tag{5}$$

where V_i is the column volume density for each sub-mode; the mean radius r_i for each sub-mode is 0.1, 0.1732, 0.3, 1.0, 2.9, and 8.4μm; and the corresponding standard deviation σ_i is 0.35,

Optics EXPRESS

0.35, 0.35, 0.5, 0.5 and 0.5, respectively. The combination of the first three sub-modes defines the fine mode particle volume distribution, and the last three sub-modes are for the coarse mode aerosols. The first five sub-mode parameters are provided by Xu et al. [28]; the sixth sub-mode is added to extend the coarse mode size for oceanic aerosols. Therefore, a total of six parameters of V_i are used to specify the aerosol volume distribution. To quantify the relative ratio between the fine mode and coarse mode, the fine mode volume fraction, f_v, is defined as $f_v = \sum_{i=1}^{3} V_i / \sum_{i=1}^{6} V_i$. Based on the six sub-mode approach, the aerosol optical depth τ_a can be defined as

$$\tau_a = \sum_{i=1}^{6} C_{ext,i} \frac{3V_i}{4\pi r_i^3} \exp(4.5\sigma_i^2) \tag{6}$$

where $C_{ext,i}$ is the extinction cross section calculated by the Mie code averaged over the i-th sub-mode volume distribution [42], and the weighting factor is to convert volume densities to number densities [47]. Both the aerosol single scattering albedo α and the aerosol backscattering fraction B_a can be calculated similarly. The aerosol backscattering fraction is defined as the ratio of the backscattering and scattering cross sections [48]. In order to compare the overall retrieval accuracy for the aerosol optical properties, we defined the aerosol backscattering optical depth as the product of the aerosol optical depth, aerosol single scattering albedo and aerosol backscattering fraction:

$$\tau_B = \tau_a \times \alpha \times B_a \tag{7}$$

Under the single scattering approximation, τ_B is equal to the irradiance reflectance, and is useful to represent the aerosol reflection property [49, 50].

The ocean surface roughness is specified by the isotropic Cox-Munk model for the wave slope distribution [51]. Wind speed is retrieved, but no wind direction is considered in the model. Whitecaps are neglected in the current model for simplicity. The free retrieval parameters associated with the atmosphere are summarized in Table 1 with the allowable maximum and minimum values and the initial values for optimization specified.

The coastal water is assumed to be homogenous with a depth of 200m, and consists of four components: pure sea water, phytoplankton covariant particles, NAP, and CDOM. CDOM only absorbs light with negligible scattering, while all other three components both scatter and absorb light. The absorption coefficient a_w and scattering coefficient b_w for pure sea water are from the experimental data [52–54].The backscattering fraction for water is 0.5 [55]. To account for the optical complexity of coastal water, we model the absorption coefficients for phytoplankton as a_{ph}, the total absorption coefficient for both CDOM and NAP as a_{dg}, the total backscattering coefficient and total backscattering fraction for both phytoplankton and NAP as b_{bp} and B_p:

$$a_{ph} = A_{ph}(\lambda)[Chla]^{E_{ph}(\lambda)} \tag{8}$$

$$a_{dg} = a_{dg}(440)\exp[-S_{dg}(\lambda - 440)] \tag{9}$$

$$b_{bp} = b_{bp}(660)(\lambda/660)^{-S_{bp}} \tag{10}$$

$$B_p = B_p(660)(\lambda/660)^{-S_{Bp}} \tag{11}$$

where λ is the wavelength in nm. a_{ph} is determined by $[Chla]$, A_{ph} and E_{ph}, where $[Chla]$ is in units of mg/m^3, and A_{ph} and E_{ph} are coefficients from [56]. S_{dg} is the exponential spectral slope for a_{dg}; S_{bp} and S_{Bp} are the polynomial spectral slopes for b_{bp} and B_p respectively (Table 2). The spectral backscattering properties of ocean water constituents are essential to the application of the ocean color remote sensing [57]. It has been demonstrated that the backscattering fraction for open ocean waters is spectrally flat [58]. However, we use a more general experession in Eq. (11) to account for coastal waters in which sediment particles may show spectral dependence.

Optics EXPRESS

The total absorption coefficient is $a = a_w + a_{ph} + a_{dg}$, and the total backscattering coefficient is $b_b = 0.5b_w + b_{bp}$. The a_{ph}, a_{dg}, and b_{bp} are the inherent optical properties that, in combination with a_w and b_w, are typically used to describe the ocean color spectrum in ocean bio-optical models [59–61].

The scattering diagrams for both phytoplankton and NAP are formulated by the Fournier-Forand (FF) phase function [62], which is consistent with a large variety of in-situ volume scattering function measurements [63]. Backscattering fraction B_{bp} is used to determine the FF phase function [64]. The FF phase function is then mixed with the pure seawater phase function to describe the total scattering diagram in the coastal water system. The total Mueller matrix is approximated by the product of the mixed phase function and the measured normalized Mueller matrix [65, 66]. There are a total of seven parameters in the bio-optical model to specify the coastal water optical properties as summarized in Table 2 with their minimum and maximum values allowed and the initial values used in retrieval.

In summary, there are eight parameters describing the imaginary and real refractive index spectra for the fine and coarse mode aerosols, five parameters describing the aerosol volume density distribution, one parameter for the wind speed, and seven parameters describing the ocean bio-optical conditions. The retrieval optimization process is to minimize the cost function and estimate the 22 retrieval parameters. In the retrieval algorithm the Jacobian matrices with respect to the retrieval parameters are calculated by the finite difference method [32], and a periodic boundary condition is implemented for all retreival parameters within the minimum and maximum allowed values as summarize in Tables 1 and 2 [67]. After the optimized retrieval parameters are obtained, the atmospheric path radiance and ocean surface reflectance will be calculated and removed from the total reflectance measured at TOA to obtain the water-leaving reflectance.

Table 1. **Retrieval parameters for aerosols and wind speed. Min., Max. and Init. are the minimum and maximum values allowed and the initial values used in retrieval.** m_r **and** m_i **are the real and imaginary refractive indices.** V_i **is the column volume density defined in Eq. (5). (*The initial** V_i **is determined by assuming aerosol optical depth of** 0.1 **with fine mode volume fraction of** 50%**.)**

Parameter	V_i	m_r	m_i	Wind speed
Unit	$\mu m^3 \mu m^{-2}$			m/s
Min.	0.0	1.1	0.0	0.0
Max.	1.0	1.6	0.03	10.0
Init.	*	1.45	0.01	3.0

Table 2. **Same as Table 1 but for the retrieval parameters of the bio-optical model as defined in Eqs. (9)-(11).**

Parameter	$[Chla]$	$a_{dg}(440)$	$b_{bp}(660)$	$B_p(660)$	S_{dg}	S_{bp}	S_{Bp}
Unit	mg/m^3	m^{-1}	m^{-1}		nm^{-1}	nm^{-1}	nm^{-1}
Min.	0.0	0.0	0.0	0.0	0.01	0.0	−0.2
Max.	30.0	2.5	0.1	0.05	0.02	0.5	0.2
Init.	15.0	1.0	0.05	0.01	0.015	0.3	0.01

3. Simulation of RSP observations

In order to validate the retrieval algorithm, and study the retrieval accuracy, synthetic RSP measurements at TOA are generated by the SOS vector radiative transfer model with various aerosol and ocean optical properties.

Optics EXPRESS

We chose the aerosol model developed by Ahmad et al., which is based on the AERONET observations in chesapeake bay [47]. In this model, the aerosol volume distribution is described by a bimodal lognormal function. Three fine mode volume fractions, f_v = 10%, 50% and 95%, are used to represent the fine mode dominated, well-mixed and coarse mode dominated cases, respectively. Two different relative humidities RH = 50% and 95% are chosen in this study. With the increase of the relative humidity, both the aerosol sizes for fine and coarse modes increases due to the hygroscopic growth of aerosols. The fine mode aerosols are weakly absorptive, where in the visible and NIR bands the albedo varies from 0.95 to 0.91 for RH = 50%, and from 0.99 to 0.98 for RH = 95%; while the coarse mode is not absorptive. To study the impact of aerosol loadings in retrieval, synthetic measurements for three aerosol optical depths τ_a(550nm) = 0.05, 0.15, and 0.3 are simulated.

To represent the complexity of the coastal water optical properties, we modeled the absorption and scattering properties for phytoplankton, CDOM and NAP randomly, while keeping the pure sea water properties the same as discussed in Section 2.2. This bio-optical model is more complicated than the bio-optical model used in the retrieval algorithm but is more accurate to represent the realistic coastal water optical properties [68, 69]. For phytoplankton, both the absorption a_{ph} and scattering coefficients b_{ph} are determined by $[Chla]$ where a_{ph} is modeled in the same way by Eq. (9). b_{ph} is determined by $b_{ph}(\lambda) = b_{ph}(660\text{nm})(\lambda/660)^k$ with $b_p(660\text{nm}) = 0.347[Chla]^{0.766}$ and the spectral slope k depending on $[Chla]$ as $k = 0$ when $[Chla] < 0.02\text{mg/m}^3$; $k = 0.5(\log_{10}[Chla] - 0.3)$ when $0.02 < [Chla] < 2\text{mg/m}^3$; and $k = 0$ when $[Chla] > 2\text{mg/m}^3$ [58]. $[Chla]$ is chosen as a random number uniformly distributed within $[0, 30]\text{mg/m}^3$. The phytoplankton scattering phase function is modeled by the FF phase function with the backscattering fraction B_{ph} determined by $[Chla]$ with no spectral dependency [58]. The CDOM absorption coefficient a_{cdom} is an exponential function similar to Eq. (9), with a_{cdom}(440nm) randomly determined for each $[Chla]$ [70], and the exponential spectral slope of of 0.018 [71].

The NAP absorption coefficient a_{nap} is also an exponential function with $a_{nap}(440\text{nm}) = 0.041[NAP]$ and the exponential spectral slope of 0.0123 [72] where $[NAP]$ is the NAP concentration in the unit of g/m^3. The NAP scattering coefficient is determined by $b_{nap} = [NAP]b^*_{nap}(\lambda)$, where the specific scattering coefficient b^*_{nap} is an inverse power law function with an empirical correction for better agreement with the measurement in the form of $b^*_{nap} = b^*_{nap}(660\text{nm})(\lambda/665)^{-(\xi_{nap}-3)} - a_{nap}(1 - \tanh(0.5 \times (\xi_{nap} - 3)^2))$ [69, 73]. b^*_{nap}(660nm) is modeled by a Junge size distribution with refractive index of 1.2 and a Junge parameter $\xi_{nap} = 4$ [69]. The NAP phase function and Mueller matrix are calculated by the Mie code averaging over the Junge distribution. $[NAP]$ is chosen as a random number uniformly distributed within $[0, 20]g/\text{m}^3$. More detailed discussions on the modeling of coastal water optical properties are in the reference [68, 69].

A total of 1800 synthetic measurements are simulated with 18 different aerosol configurations and 100 different combinations of $[Chla]$, $[NAP]$ and a_{cdom}(440nm) in the bio-optical model. An incident solar zenith angle of 30° is used in the simulation. Random noise is added to the synthetic measurements according to the noise model in Eq. 4. We emphasize that the aerosol and ocean bio-optical models used in the synthetic RSP simulation are different from that of the retrieval algorithm described in Sec. 2 in order to mimic the retrieval of real measurements, for which the truth is unknown and likely different from the inherent optical properties used. The achieved goodness of the retrieval shown in the following discussion demonstrates that our retrieval algorithm is robust and flexible in terms of aerosol and hydrosol properties.

4. Synthetic retrieval results and discussions

In this validation effort the synthetic measurement data are the input to the retrieval algorithm. The retrieval parameters are obtained by minimizing the cost function which measures the

Optics EXPRESS

difference of the modeled and the synthetic measurements for ρ_t and ρ_Q. The success rate is defined as the cumulative probability of all the retrieval cases with a cost function value less than a critical value χ_c^2. We choose $\chi_c^2 = 3$ for our discussion which corresponds to a success rate of nearly 90% as shown in Fig. 2. Choosing a larger χ_c^2 will improve the success rate but may decrease the retrieval accuracy. With $\chi_c^2 = 3$, the difference between the true and retrieved wind speed is less than 0.5m/s approximately as shown in Fig. 3. When comparing the converged cost function values for different volume distributions, the coarse mode dominated cases have slightly larger values than the fine mode dominated cases. This may relate to the larger uncertainty in the wind speed retrieval for the coarse mode dominated cases compared with the fine mode dominated cases. In the following we will discuss the accuracy of the retrieved aerosol properties, water-leaving reflectance ρ_w^{TOA}, and the ocean optical properties.

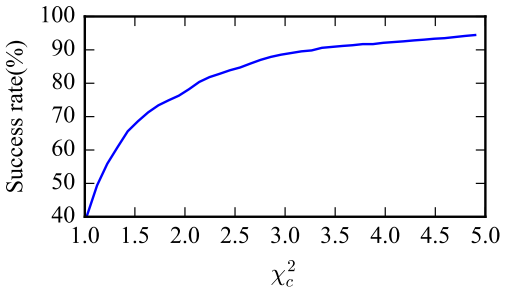

Fig. 2. The success rate with respect to the critical cost function value χ_c^2.

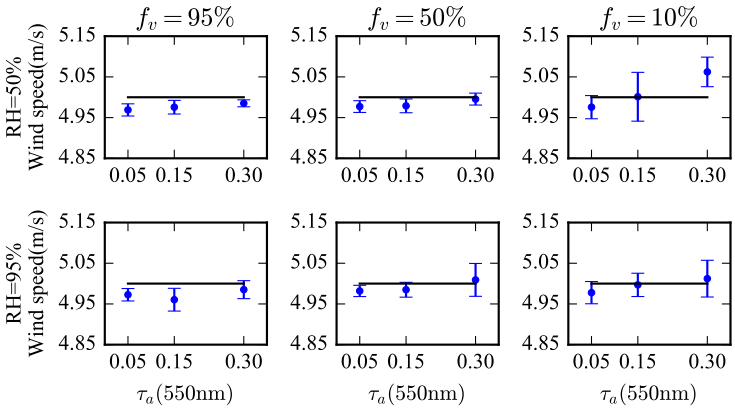

Fig. 3. The retrieved and true wind speed are compared for fine mode volume fraction f_v = 95%, 50% and 10% and the relative humidity RH = 50% and 95%, and aerosol optical depth τ_a(550nm)=0.05, 0.15 and 0.3. The vertical bar shows the retrieval uncertainty determined through the variation of retrieved values. Solid line incidates the true wind speed value of 5m/s.

4.1. *Aerosol microphysical and single scattering properties*

The accuracy of the retrieved aerosol microphysical properties, including the aerosol volume distribution and aerosol refractive index spectra, depends on the aerosol optical depth (τ_a), fine mode volume fraction (f_v), and relative humidity (RH) as shown in Figs. 4 and 5 and Table 3.

Optics EXPRESS

The aerosol single scattering properties are calculated by the aerosol microphysical properties as shown in Figs. 6-9. The single scattering optical properties include the aerosol optical depth, albedo, backscattering fraction, and backscattering optical depth as defined in Eq. (7).

Both the volume distribution and the aerosol refractive index spectrum are constructed directly through the retrieved model parameters. Since the mathematical expressions for the retrieved and true volume distributions are different, where the true distribution is a bimodal lognormal function and the retrieved one is a combination of six different lognormal functions, the retrieved effective radii [41] and their standard deviation are calculated in order to compare with the input values as shown in Table 3. Both Fig. 4 and Table 3 show that fine mode volume distribution is more accurately retrieved when the fine mode volume fraction dominates. The standard deviation of the effective radius generally decreases with the increase of aerosol optical depth. The fine mode effective radius ($r_{eff,f}$) is retrieved with uncertainty less than 0.02μm for RH = 50%. For the coarse mode effective radius ($r_{eff,c}$) at the same relative humidity, the maximum retrieval uncertainty increases to 0.66μm.With the increase of relative humidity from RH = 50% to RH = 95%, the maximum retrieval uncertainty for $r_{eff,f}$ increases to 0.04μm and for $r_{eff,c}$ it increases to 1.02μm due to the increased aerosol sizes.

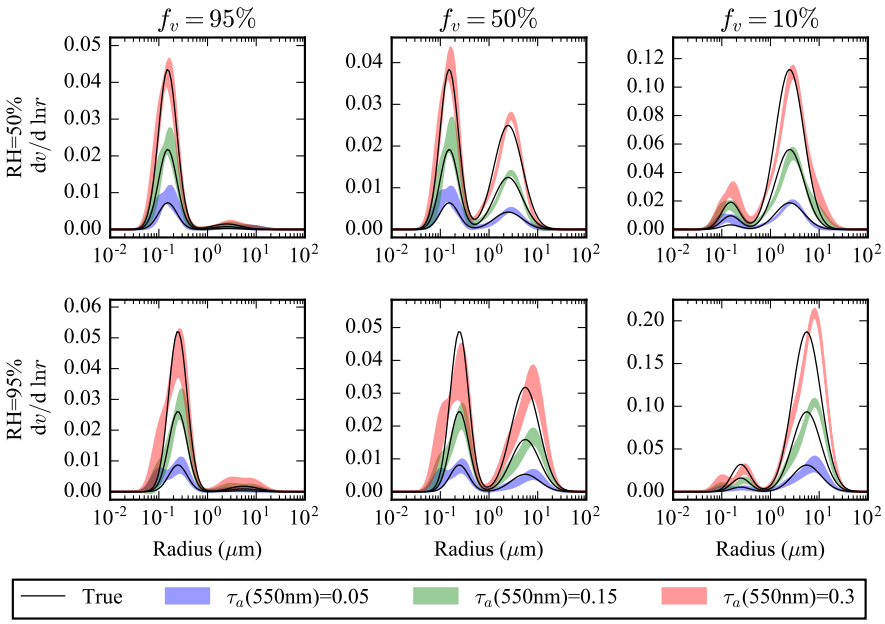

Fig. 4. The retrieved and true aerosol size distribution comparison for the same cases shown in Fig. 3. The true aerosol size distribution are shown in black. The retrieval results for three different optical depths are shown in blue, green and red, where the vertical variations represent the retrieval uncertainty.

The retrieval uncertainty of the refractive index spectra for both the fine and coarse modes also depends on their volume fraction. To account for the volume fraction dependency, the volume-averaged refractive index is defined as $m_v = f_v m_f + (1 - f_v)m_c$ and is shown in Fig. 5. For the fine mode dominated case, the retrieved refractive indices tend to be smaller than the true values, but for the coarse mode dominated cases they tend to be larger than the true values. This trend is similar to the effective radius comparison shown in Fig. 4. Larger aerosols generally have smaller backscattering fraction due to stronger forward scattering, which can be compensated by the increase of refractive index. The retrieval accuracy also depends on the aerosol loadings. The

Optics EXPRESS

Table 3. **The true and retrieved effective radii for fine mode ($r_{eff,f}$) and coarse mode ($r_{eff,c}$) in μm derived from the aerosol size distributions shown in Fig. 4. The first row for each RH case shows the true effective radii.**

		f_v=95%		f_v=50%		f_v=10%	
RH	$\tau_a(550nm)$	$r_{eff,f}$	$r_{eff,c}$	$r_{eff,f}$	$r_{eff,c}$	$r_{eff,f}$	$r_{eff,c}$
50%	(true)	0.14	1.98	0.14	1.98	0.14	1.98
	0.05	0.14±0.02	3.02±0.66	0.13±0.02	2.11±0.16	0.12±0.02	1.98±0.06
	0.15	0.14±0.01	2.68±0.57	0.14±0.02	1.96±0.07	0.13±0.01	2.12±0.10
	0.3	0.13±0.01	2.45±0.31	0.13±0.01	1.93±0.03	0.14±0.02	2.11±0.05
95%	(true)	0.22	4.43	0.22	4.43	0.22	4.43
	0.05	0.17±0.03	3.34±1.02	0.18±0.04	4.80±0.79	0.16±0.04	4.48±0.75
	0.15	0.22±0.03	3.55±0.88	0.20±0.03	4.74±0.42	0.18±0.03	4.91±0.21
	0.3	0.19±0.03	3.57±0.59	0.17±0.03	4.71±0.49	0.18±0.03	4.96±0.16

maximum difference between the retrieved and true refractive indices decreases with aerosol optical depth: it can be as large as 0.07 for τ_a(550nm) = 0.05 but reduces to less than 0.03 for τ_a(550nm) = 0.3 regardless of the volume fractions, relative humidity and wavelengths shown in Fig. 5. In the visible and NIR bands, the differences between retrieved and true refractive indices are smaller than 0.01 for RH = 50%, but increase to 0.03 for the relative humidity of 95%.

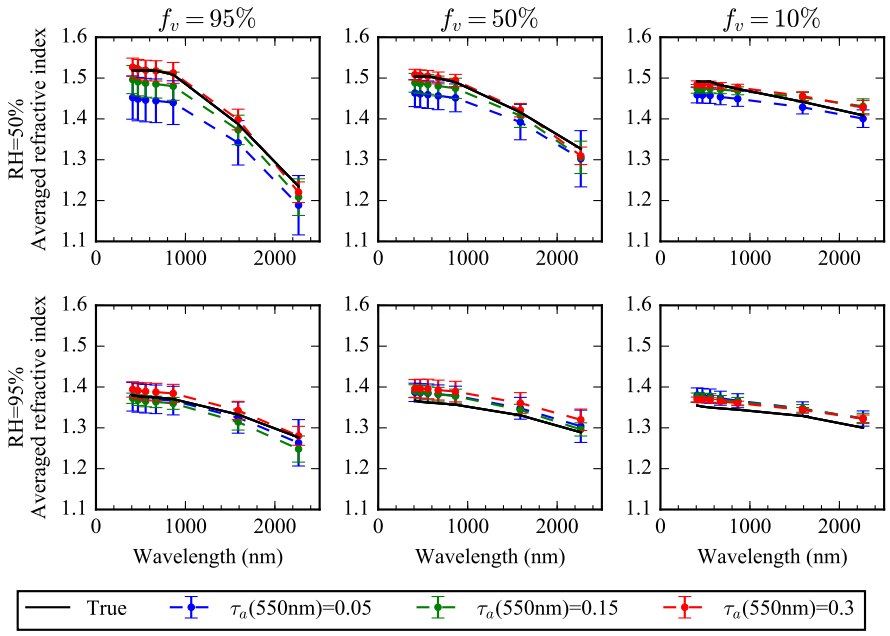

Fig. 5. The comparison between the retrieved and true volume averaged refractive indices for the same cases shown in Fig. 3.

Figure 6 shows the performance of aerosol optical depth retrieval, which is more accurate in the visible and NIR bands comparing with the retrieval in the SWIR. For the coarse mode dominated cases, the retrieved optical depth is smaller than the true one in SWIR while for the fine mode dominated cases, the retrieval results over estimate the aerosol optical depth in SWIR. With aerosol optical depth at 550nm varying from 0.05 to 0.3, the maximum percentage difference between the retrieved and true τ_a in the visible and NIR bands decreases from 25% to

Optics EXPRESS

4%, while in SWIR the percentage difference are much larger with values from 80% to 25%. The larger inaccuracy of τ_a in SWIR is associated with the smaller aerosol optical depth as compared with the visible bands, especially for the fine mode dominated cases.

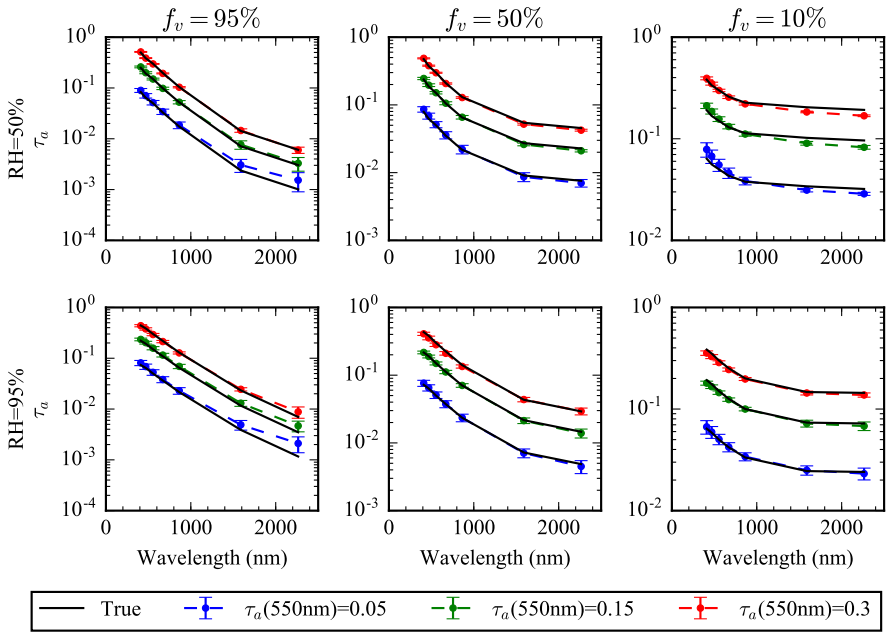

Fig. 6. The retrieved and true aerosol optical depth(τ_a) for the same cases as in Fig. 3.

Figure 7 shows the aerosol single scattering albedo comparison. Across the whole spectra from visible to the SWIR bands, the true aerosol single scattering albedo for fine mode dominated cases varies from 0.98 to 0.54; while for both the coarse mode dominated and well mixed cases, the aerosol single scattering albedo ranges between 0.99 and 0.92. The retrieval error is more prominent in the fine mode dominated cases: for aerosol optical depth τ_a(550nm) = 0.05 the maximum percentage is 4% in the visible and NIR, and up to 28% in the SWIR. The difference reduces to 4% for τ_a(550nm) = 0.3 in SWIR. For the well-mixed and coarse mode dominated cases, the difference is generally within 6% for all aerosol loadings considered in this study.

The backscattering fraction (B_a) quantifies the reflection strength of a single scatter. Fine mode aerosols backscatter much stronger than the coarse mode aerosols, as shown in Fig. 8, where B_a can be as large as 27% for the fine mode dominated case, but it is less than 10% for coarse mode dominated case. Further for fine mode dominated case, there are large spectral dependencies in the visible and NIR bands: for RH = 50%, B_a varies from 5% to 20%; while for coarse mode dominated case, B_a is within 5% to around 10%. The percentage difference between the retrieved and true values is smaller than 10% for RH = 50%, but the maximum difference increases to 30% for RH = 95%. There is larger retrieval inaccuracy associated with small aerosol loading. For the fine mode dominated cases with τ_a = 0.05, the retrieved B_a is significantly under estimated in the SWIR bands, while for the well-mixed and coarse mode dominated cases with the same optical depth, the retrieval tends to be overestimated slightly. Due to the large spectral variations in the visible bands, the water-leaving reflectance retrieval is sensitive to the accuracy of the backscattering fraction estimation.

The retrieval errors for the aerosol optical depth, single scattering albedo, and the single scattering backscattering fraction compensate each other. With RH = 50%, f_v = 95% and

Optics EXPRESS

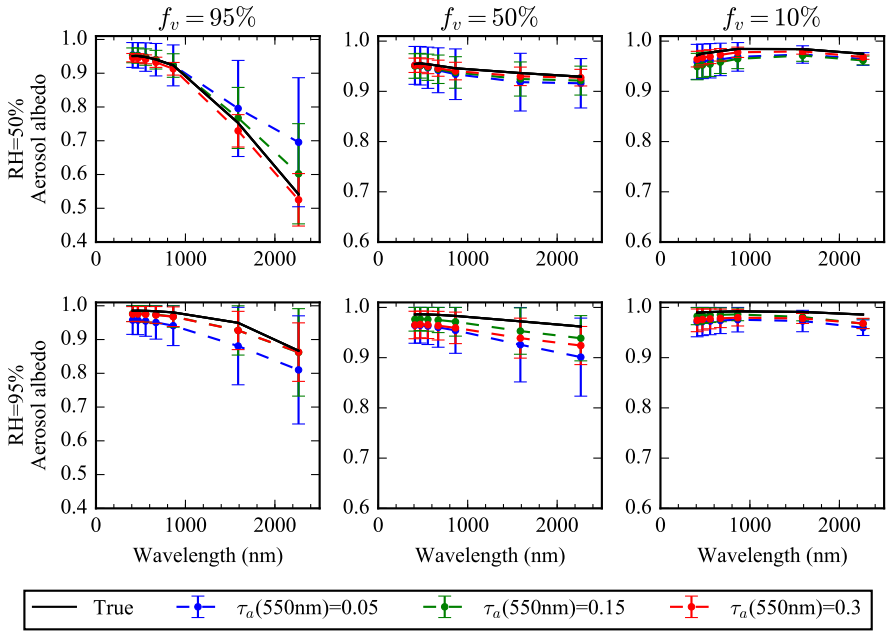

Fig. 7. Same as Fig. 3 but for the aerosol single scattering albedo.

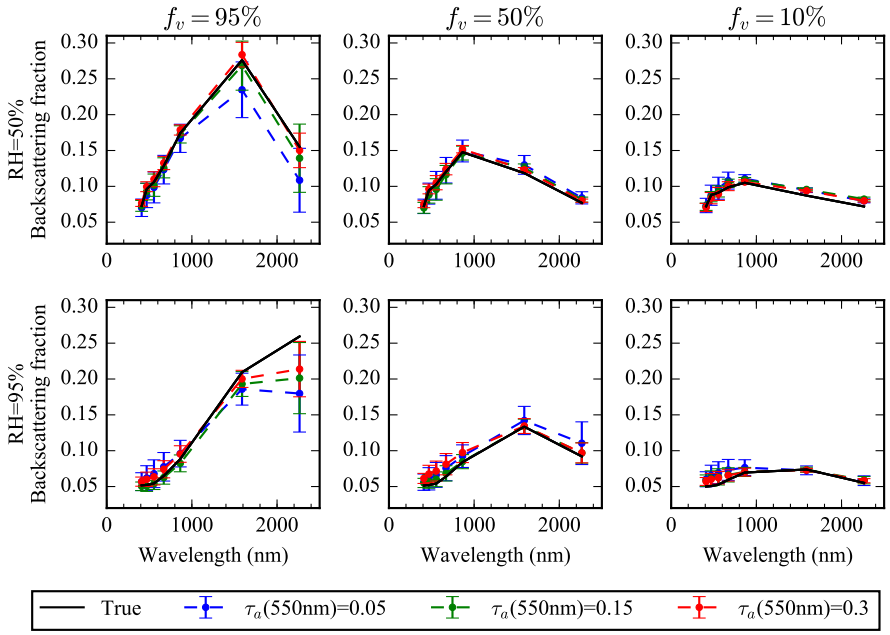

Fig. 8. Same as Fig. 3, but for the aerosol backscattering fraction.

τ_a = 0.05, for example, the retrieved aerosol backscattering fraction is smaller than the true value in SWIR but both the retrieved albedo and optical depth are larger than the true value. Therefore, the smaller backscattering is compensated by the larger aerosol loading and less

Optics EXPRESS

absorption. To study this dependency, the backscattering optical depth τ_B is shown in Fig. 9. The backscattering optical depth defined by Eq. (7) is the product of the optical depth, albedo, and the backscattering fraction. For RH = 50% in the whole spectral range, the maximum percentage difference between the retrieved and true τ_B is around 23% for τ_a(550nm) = 0.05 and it reduces to less than 7% and 8% for τ_a = 0.15 and τ_a = 0.3. Within the visible and NIR bands, the retrieval difference generally reduces with aerosol loadings: for τ_a(550nm) = 0.05, 0.15 and 0.3 the averaged percentage difference are 10%, 2% and 4%. While for RH = 95% in the whole spectral range, the maximum percentage difference is around 30% for τ_a(550nm) = 0.05 and it reduces to less than 15% and 20% for τ_a = 0.15 and τ_a = 0.3 as shown in Fig.10. Except in the SWIR bands for f_v = 95% where the optical depth is very small, the major percentage difference between the retrieved and the true backscattering optical depth is in the visible bands, and it appears correlating with the spectral shape of the water-leaving reflection spectrum(see Fig. 11 in the next subsection). This is due to the imperfect separation of the aerosol and water-leaving signals at the TOA. Since the SWIR bands are free from the influence of the water-leaving reflection, the retrieval in the SWIR bands is more accurate with the percentage difference below 20%, 4% and 1% for τ_a(550nm) = 0.05, 0.15 and 0.3 respectively.

With the retrieved aerosol refractive index spectrum and volume distribution, the aerosol path radiance can be calculated and used to obtain the water-leaving reflectance for the atmospheric correction. Further, although we observe large error in the aerosol property retrieval for small aerosol optical depth, the water-leaving radiance reflectance is not very sensitive to the inaccuracy of the aerosol properties for small optical depth because the aerosol path radiance is also small in this case.

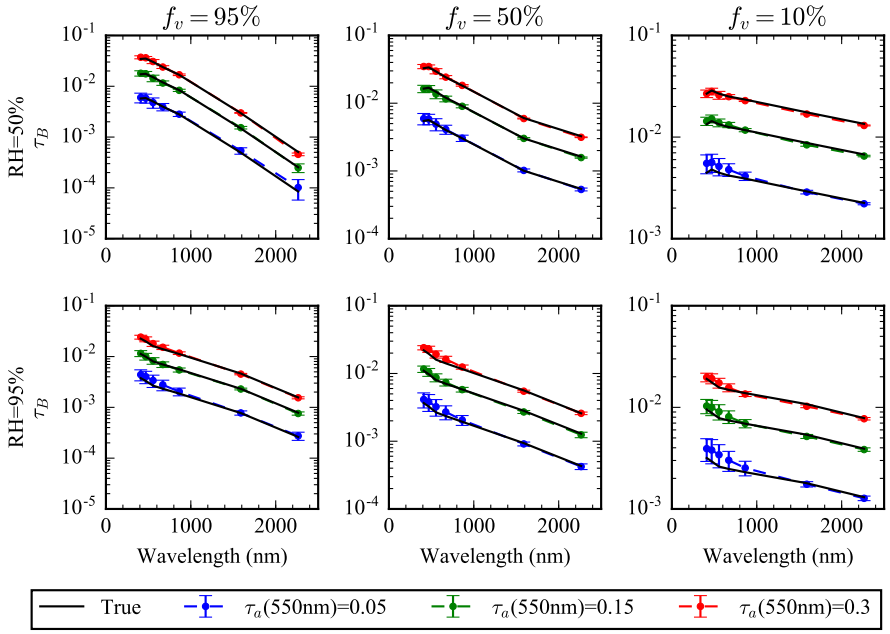

Fig. 9. Same as Fig. 6 but for the aerosol backscatteing optical depth τ_B defined in Eq. (7).

4.2. *Water-leaving reflectance and ocean optical properties*

The magnitude and spectral shape of the water-leaving reflectance varies depending upon the optical properties of phytoplankton, NAP, and CDOM. Figure 11 show the water-leaving

Optics EXPRESS

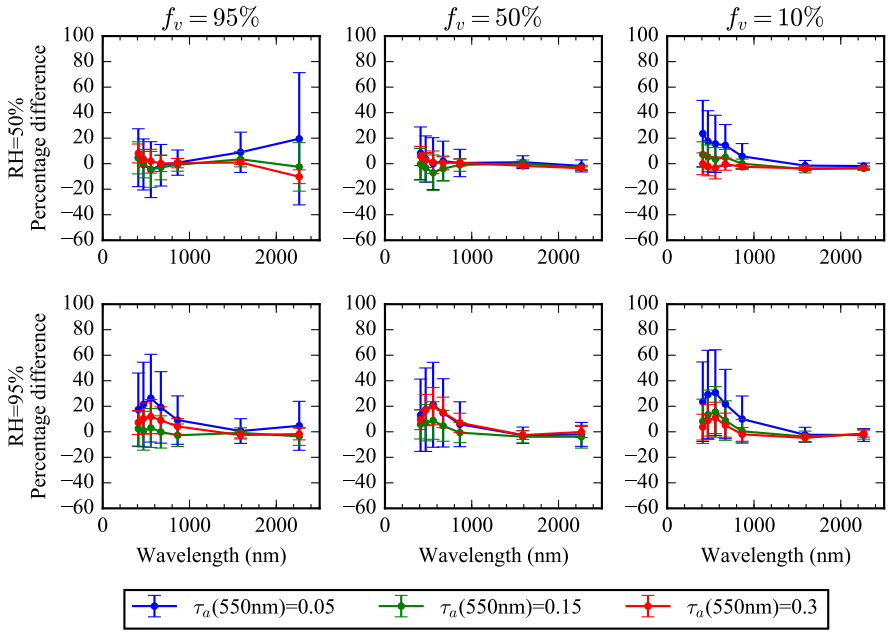

Fig. 10. Same as Fig. 9 but for percentage difference between the retrieved and true backscattering optical depth.

reflectance and the percentage fraction of the water-leaving signal in the total reflectance at TOA for τ_a(500nm)=0.15, RH = 50% and f_v = 50%. The water-leaving reflectance at other RH and f_v share similar spectral variations. The waterleaving signal can be up to around 25% in the total signal, which requires an accurate bio-optical model to account for its contribution.

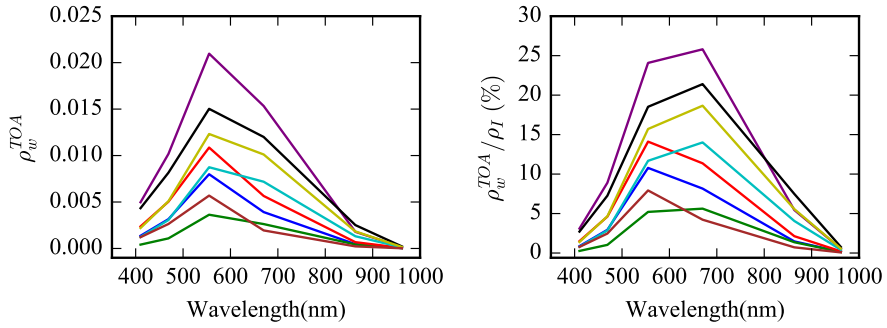

Fig. 11. Examples of the TOA water-leaving reflectance spectra (ρ_a^{TOA}) and its percentage in the total reflectance ($100 \times \rho_w^{TOA}/\rho_I$) for τ_a(550nm) = 0.15, RH = 50% and f_v = 50%.

The retrieved and true TOA water-leaving reflectance is compared in Figs. 12, 13 and 14 for wavelengths from 410nm to 865nm and τ_a(550nm) = 0.05, 0.15 and 0.3, respectively. The correlation (corr), root mean square difference(RMS), and the linear fitting regression are also shown. The retrieval accuracy decreases as the aerosol optical depth increases. With τ_a(550nm) = 0.05, 0.15 and 0.3, the maximum RMS increases from 0.0008 and 0.0011 to 0.0013. The maximum fitting bias also varies; for all the cases, the fitting bias is less than 0.0003.

Optics EXPRESS

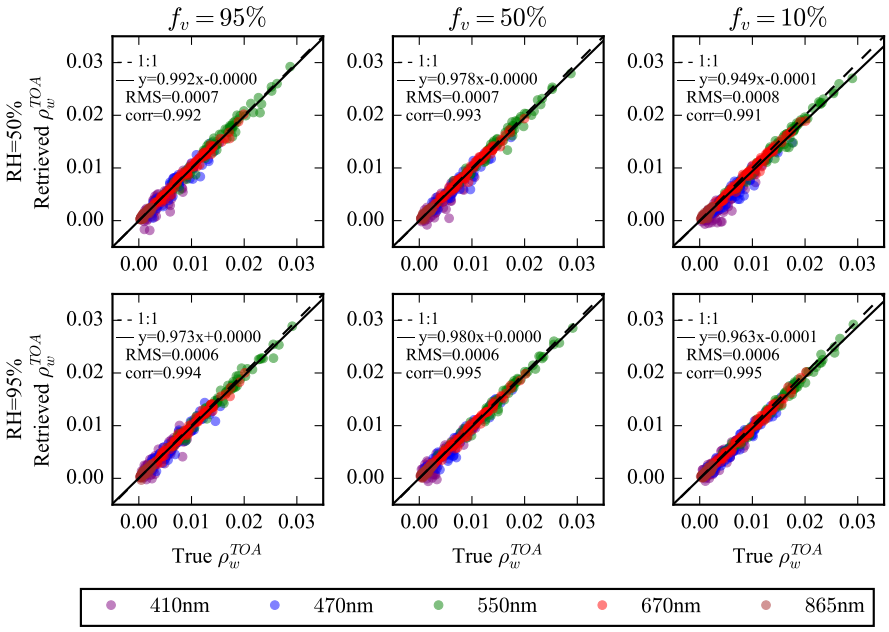

Fig. 12. The comparison between the true and retrieved TOA water leaving signal (ρ_w^{TOA}) for τ_a(550nm) = 0.05.

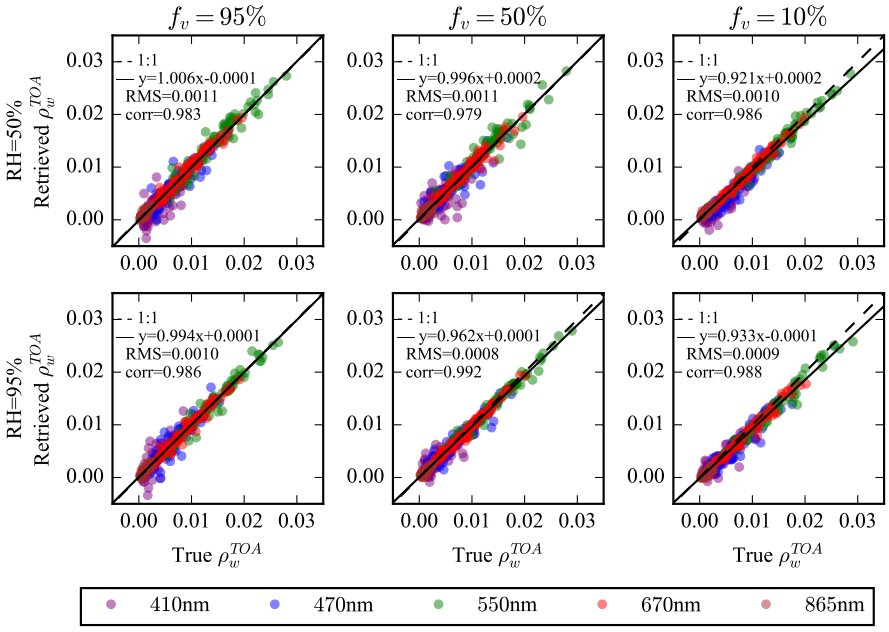

Fig. 13. Same as Fig. 12 but with τ_a(550nm) = 0.15.

The retrieved and true water-leaving reflectance are also compared for individual wavelength of 410nm, 550nm and 670nm, respectively in Tables 4, 5, and 6. The largest variation in the retrieval

Optics EXPRESS

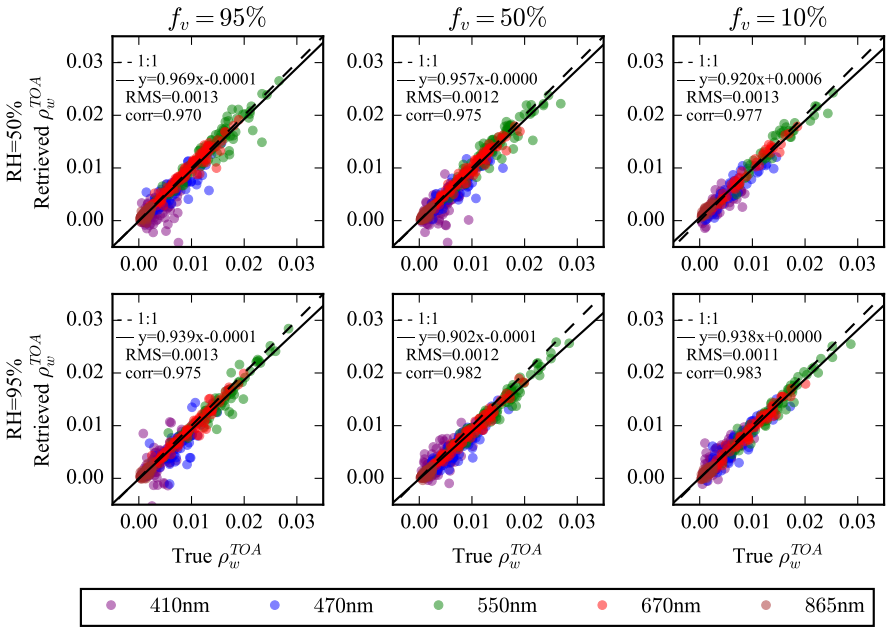

Fig. 14. Same as Fig. 12, but with τ_a(550nm) = 0.3.

Table 4. **The comparison between the true and retrieved TOA water leaving signal in terms of fitting slope, bias, correlation, and RMS for band** 410**nm,** 550**nm and** 670**nm and** τ_a(550**nm**) = 0.05 **same as Fig. 12. The first column shows the fine mode volume fraction (**f_v**).**

f_v	wavelength	410nm		550nm		670nm	
	RH	50%	95%	50%	95%	50%	95%
95%	slope	0.9373	0.9138	0.9962	0.9696	0.9851	0.9851
	bias	-0.0003	0.0001	0.0001	0.0002	0.0001	0.0001
	corr	0.8868	0.9015	0.9897	0.9924	0.9933	0.9943
	RMS	0.0012	0.0011	0.0008	0.0007	0.0005	0.0005
50%	slope	0.8547	0.9620	0.9745	0.9814	0.9798	0.9798
	bias	-0.0001	-0.0001	0.0002	0.0001	0.0001	0.0001
	corr	0.8873	0.9152	0.9906	0.9931	0.9934	0.9950
	RMS	0.0010	0.0010	0.0007	0.0007	0.0005	0.0004
10%	slope	0.8702	0.9194	0.9740	0.9790	0.9830	0.9830
	bias	-0.0007	-0.0002	-0.0002	-0.0002	-0.0002	-0.0002
	corr	0.9005	0.9341	0.9920	0.9943	0.9944	0.9953
	RMS	0.0010	0.0009	0.0007	0.0006	0.0005	0.0004

results appears from the band of 410nm with maximum RMS of 0.0012, 0.0017 and 0.0022, and minimum correlation of 0.887, 0.6 and 0.516 for τ_a(550nm) = 0.05, 0.15 and 0.3, respectively. The retrieved value can become negative occasionally for 410nm when the fitted atmospheric path radiance is slightly larger than the total measured radiance at TOA. The variation decreases when the wavelength increases to 550nm with a maximum RMS of 0.0017 and a minimum correlation of 0.941 at τ_a(550nm) = 0.3.

The retrieval accuracy for the water-leaving reflectance correlates with that of the aerosols.

Optics EXPRESS

Table 5. **Same as Table 4 but for τ_a(550nm) = 0.15 and Fig. 13.**

f_v	wavelength	410nm		550nm		670nm	
	RH	50%	95%	50%	95%	50%	95%
95%	slope	0.8513	1.0618	1.0095	1.0069	1.0088	1.0088
	bias	-0.0004	-0.0003	0.0001	-0.0002	0.0001	0.0001
	corr	0.7580	0.8064	0.9732	0.9820	0.9854	0.9866
	RMS	0.0017	0.0017	0.0013	0.0010	0.0007	0.0007
50%	slope	0.6210	0.7768	0.9570	0.9581	0.9668	0.9668
	bias	0.0009	0.0006	0.0010	0.0003	0.0006	0.0006
	corr	0.6000	0.8243	0.9651	0.9896	0.9791	0.9924
	RMS	0.0018	0.0013	0.0013	0.0008	0.0008	0.0005
10%	slope	0.8666	0.8379	0.9765	0.9584	0.9747	0.9747
	bias	-0.0007	0.0001	-0.0003	-0.0004	-0.0001	-0.0001
	corr	0.8712	0.8436	0.9901	0.9848	0.9937	0.9889
	RMS	0.0012	0.0014	0.0008	0.0010	0.0005	0.0007

Table 6. **Same as Table 4 but for τ_a(550nm) = 0.3 and Fig. 14.**

f_v	wavelength	410nm		550nm		670nm	
	RH	50%	95%	50%	95%	50%	95%
95%	slope	0.5341	0.8619	0.9348	0.9481	0.9683	0.9683
	bias	0.0001	-0.0002	0.0008	-0.0001	0.0004	0.0004
	corr	0.5157	0.6631	0.9406	0.9671	0.9719	0.9788
	RMS	0.0020	0.0022	0.0017	0.0014	0.0010	0.0009
50%	slope	0.5686	0.7273	0.9263	0.9194	0.9586	0.9586
	bias	0.0002	0.0006	0.0008	-0.0002	0.0003	0.0003
	corr	0.5501	0.6839	0.9535	0.9787	0.9820	0.9854
	RMS	0.0020	0.0019	0.0015	0.0011	0.0008	0.0008
10%	slope	0.6426	0.8377	0.9320	0.9664	0.9886	0.9886
	bias	0.0006	0.0009	0.0009	-0.0004	0.0001	0.0001
	corr	0.6683	0.7526	0.9658	0.9762	0.9857	0.9840
	RMS	0.0018	0.0017	0.0013	0.0012	0.0007	0.0008

For example, the fitting slope reaches its minimum value of 0.912, for RH = 95%, f_v = 50% and τ_a(550nm) = 0.3, which corresponds with the largest percentage difference for the backscattering optical depth of 20% at wavelength of 550nm. Generally if the maximum percentage difference for the backscattering optical depth is less than 10%, the fitting slopes can be close to 1.0 with a difference smaller than 4%. The root mean square difference in the retrieved water-leaving reflectance also correlates to the root mean square difference of the backscattering optical depth. The maximum root mean square difference of the backscattering optical depth between the retrieved and true values is in the band of 410nm for each f_v and RH. For the case of RH = 95% and f_v = 50% as example, the root mean square differences of the backscattering optical depth are 0.0010, 0.0013 and 0.0019 for τ_a(550nm) = 0.05, 0.15 and 0.3, respectively. This is in agreement with the root mean square difference for the water-leaving reflectance with values from 0.0010, 0.0013, and 0.0017 for the same three aerosol loading, f_v and RH.

The retrieved water-leaving reflectance is obtained by removing the total aerosol, molecule, and ocean surface contributions from the total signal. If in the retrieval optimization process the water-leaving signal is not well represented by the bio-optical model, the signals may be incorrectly attributed to the aerosol contributions. Here we compare the retrieved and true

Optics EXPRESS

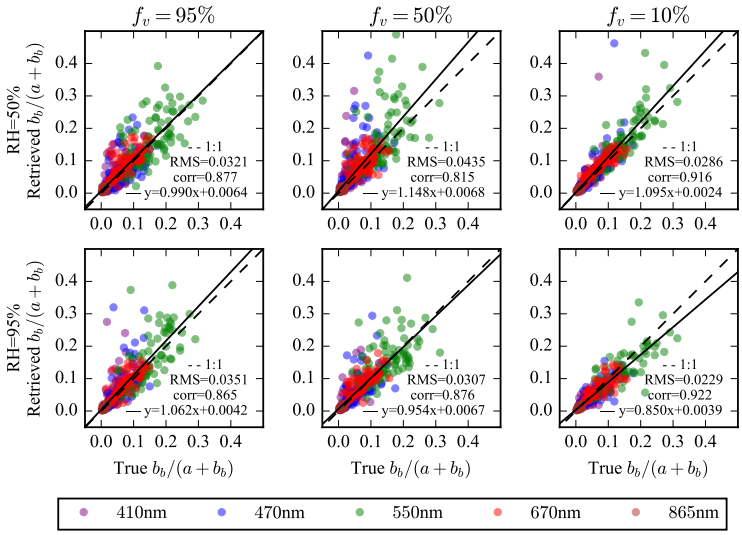

Fig. 15. The comparison between the retrieved and true $b_b/(a + b_b)$ for τ_a(550nm) = 0.15.

$b_b/(a + b_b)$ to study the accuracy of the retrieved ocean optical properties. Here a is the total absorption coefficient, and b_b is the backscattering coefficient. $b_b/(a + b_b)$ relates to the total upwelling irradiance just below the ocean surface [74]. The comparison for τ_a(550nm) = 0.15 in the visible and NIR bands is shown in Fig. 15. For fine mode dominated and well mixed cases, the correlation is lower than 0.877 for both RH = 50% and RH = 95%. The correlation increases to above 0.90 for the coarse mode dominated case. This suggests that the influence of the coarse mode aerosol retrieval in the water-leaving reflectance retrieval is smaller than the fine mode influence. The minimum correlation between the retrieved and true $b_b/(a + b_b)$ is 0.815. The validation results of $b_b/(a + b_b)$ suggests that the generalized bio-optical model in the retreival algorithm well characterizes the near-surface marine optical properties. The correlation for the water-leaving reflectance is higher than that of $b_b/(a + b_b)$ as shown in Fig. 13, where the minimum correlation is 0.979. This may be due to the fact that the reflectance signal differences are directly measured by the cost function, while $b_b/(a + b_b)$ is retrieved indirectly from the water-leaving signals, which are not completely determined by $b_b/(a + b_b)$ due to effects such as under water multiple scatterings, air-sea transmittance, and the sea surface bidirectional reflectance distribution function(BRDF).

To evaluate the ocean biological conditions, $[Chla]$ is an important quantity in the bio-optical retrieval after the atmospheric correction [59]. In our retrieval algorithm, $[Chla]$ is used as one componet to constrain the total absorption and scattering coefficients in the retrieval optimization process. The retrieval results show that the correlation between the retrieved and true $[Chla]$ is lower than 0.2 for all retrieval cases (figure not shown). The correlations between the retrieved and true values for a, and b_b are around 0.8 and 0.6, respectively. Both values are significantly larger than the correlation for $[Chla]$. This is because the total absorption is determined by multiple components of the coastal waters including phytoplankton, CDOM, and NAP. There is not enough sensitivity contained in the cost function to precisely separate the contributions from phytoplankton, CDOM and NAP. The goal of the current algorithm is not to derive precise in-water properties directly, but to better characterize the atmosphere using a more realistic ocean model. The aerosol properties retreived from a multiangle polarimeter may be applied to an extended spectral range for an ocean color instrument and provide a better atmospheric correction

Optics EXPRESS

which in turn improve the derivation of $[Chla]$ and the other biogeochemical conditions of coastal waters. The influence of the inelastic scattering mechanisms in the retrieval will be evaluated in the future work, including the contributions from Raman scattering, fluorescence by colored dissolved organic matter (FDOM), and fluorescence by chlorophyll [39].

5. Conclusions

A joint retrieval algorithm for both aerosol and ocean water optical properties is developed for a coupled atmosphere and ocean system over complex coastal waters. The retrieval algorithm is optimized to obtain accurate water-leaving reflectance for the purpose of atmospheric correction. The retrieval algorithm includes 22 parameters, which describes the aerosol refractive index spectra, aerosol volume size distribution, wind speed, and the ocean water bio-optical model. The ocean water bio-optical model is generalized for coastal waters with direct accounting of the absorption and scattering for pure sea water, phytoplankton, CDOM, and NAP. The retrieval accuracy of the aerosol refractive index, aerosol volume distribution, optical depth, albedo and the backscattering fraction are discussed for various aerosol optical depths, relative humidity and fine mode volume fractions. The retrieval errors for the aerosol optical depth, albedo, and backscattering fraction compensate each other.

Despite the different bio-optical model assumptions used in the synthetic data generation and retrieval algorithm, the water-leaving reflectance is well retrieved with the correlation coefficients over 0.97 with the true value, a bias smaller than 0.0006 and a root mean square difference around 0.001. The water-leaving reflectance can contribute significantly to the total reflectance at TOA for coastal waters, and causes strong dependency of the retrieval accuracy between the aerosol and ocean optical properties. The retrieved water-leaving reflectance and its uncertainties are discussed for different aerosol loadings, and realtive humidity and fine mode volume fractions. The relationship with the retrieved aerosol properties is also discussed through the aerosol backscattering optical depth. Both the aerosol and ocean optical properties need to be accurately modeled in order to achieve better retrieval for each other.

The retrieval accuracy for ocean optical properties is studied through $b_b/(a+b_b)$. The retrieved $b_b/(a+b_b)$ is compared with the true value with a correlation of approximately 0.8. This suggests that the ocean bio-optical model provides a good constraint on the ocean leaving signals, which can help to improve the estimation of aerosol properties. The determination of $[Chla]$ is, however, less reliable because different combinations of CDOM, NAP and phytoplankton could lead to similar water leaving radiance. The aerosol properties retrieved in our algorithm may be used to perform atmospheric correction for a co-located hyperspectral radiometer, which can provide more information on biogeochemical condition of ocean waters.

Acknowledgments

Pengwang Zhai is partially supported by the NASA PACE Project. This study is also partially supported by the NASA Radiation Science program administrated by Hal Maring and the Biology and Biogeochemistry program administrated by Paula Bontempi.

The hardware used in the computational studies is part of the UMBC High Performance Computing Facility (HPCF). The facility is supported by the U.S. National Science Foundation through the MRI program (grant nos. CNS–0821258, CNS–1228778, and OAC–1726023) and the SCREMS program (grant no. DMS–0821311), with additional substantial support from the University of Maryland, Baltimore County (UMBC). See hpcf.umbc.edu for more information on HPCF and the projects using its resources.

Funding

NASA (NNX15AB94G, NNX15AK87G and 80NSSC18K0345).